The effect of high viscosity on the evolution of the bifurcation set of a periodically excited gas bubble

Kálmán Klapcsik[a,*], Ferenc Hegedűs[a]

[a]*Department of Hydrodynamic Systems*
Faculty of Mechanical Engeneering
Budapest University of Technology and Economics
P.o. Box 91. 1521, Budapest, Hungary

Abstract

In this study, a nonlinear investigation of a periodically driven gas bubble in glycerine is presented. The bifurcation structure of the bubble oscillator (Keller–Miksis equation) is explored in the pressure amplitude-frequency parameter plane of the excitation by means of initial (high resolution bi-parametric plots) and boundary value problem solvers at various ambient temperatures. The range of the applied temperature covers two orders of magnitude difference in the liquid viscosity which is the main damping factor of the system. Therefore, the evolution of the harmonic and ultraharmonic resonances are presented starting with an overdamped behaviour (there are no resonances in the parameter space) and ending up with a fully developed bifurcation superstructure. The results reveal a complex period bubbling mechanism organized in a Farey-tree; inside each bubble a fine substructure of alternating chaotic and periodic bands exist. The description of the bifurcation structure presented throughout the paper can help to understand the mechanism of dissipation on the behaviour of nonlinear systems in more detail.

Keywords: Bubble dynamics, Bifurcation structure, Dissipation mechanism, Keller–Miksis equation, Bi-parametric maps, Farey-tree, GPU accelerated IVPs

*Corresponding author
Email addresses: kklapcsik@hds.bme.hu (Kálmán Klapcsik), fhegedus@hds.bme.hu (Ferenc Hegedűs)

1. Introduction

The interaction of high intensity and high frequency sound waves with liquid domains can lead to the phenomenon called acoustic cavitation, which produces bubble clusters. These are usually composed by micron-sized gas bubbles oscillating around their equilibrium size. When the intensity reaches Blake's threshold [1], the bubbles become cavitationally active, and start to oscillate with high amplitude. During the radial oscillation of such bubbles, at the minimum bubble radius (collapse phase), the temperature and pressure in the bubble interior can exceed thousands of Kelvin and bar, respectively [2]. Cavitationally active bubbles always grow by rectified diffusion [3–6] due to the much larger diffusive area at the expansion phase than at the collapse phase. The limit of the growth is the size where the bubble lose its spherical stability [7, 8]. Spherically unstable bubbles disintegrate into smaller bubbles, which start to grow again by rectified diffusion, or dissolve into the liquid domain. This process is called bubble life cycle, for the details see [9–11].

The time scale of the life cycle of a bubble is greater by many orders of magnitude than the period of its radial oscillation. Therefore, it is reasonable to investigate a single individual bubble as a building block of clusters. The dynamics of such bubbles shows highly nonlinear properties. Modern numerical techniques and methods of chaos physics revealed the existence of harmonic and subharmonic resonances in the pressure amplitude-frequency plane [12–19], the presence of period-doubling route to chaos [20–25] and the alteration of chaotic and periodic windows [26–29] in the bifurcation pattern. The majority of these nonlinear features have already been proven experimentally. Subharmonics in the spectrum of the response of a bubble was observed first by Esche [30]. Later, Lauterborn and his co-workers successfully justified the existence of period-doubling route to chaos in water [31, 32]. Chaotic bubble oscillation was also found by high-speed holographic cinematography [33], and by measuring the time delays between flashes of emitted light (sonoluminescence [34–36]) at the collapse phase of a bubble [37].

The aforementioned knowledge accumulated over decades in nonlinear bubble dynamics is usually related to water (few exceptions are [38–41]). Therefore, the present study intends to investigate a gas bubble in glycerine with varying temperature (between 20 °C and 70 °C); that is, the viscosity is varied between two orders of magnitude (see Tab. C.2) leading to three

to one orders of magnitude higher values than of water. It is well-known that high viscosity causes huge damping effect [42, 43], which implies a much less feature-rich bubble dynamics. Throughout this paper, the evolution of the bifurcation structure in the pressure amplitude-frequency plane with decreasing damping factor is examined and compared with results obtained on other nonlinear oscillators such as Toda [44], Duffing [45–47], Morse [48] and bubbles in water (see the discussion above).

The applied bubble model is the Keller–Miksis equation, which is a second order ordinary nonlinear differential equation that takes into account the compressibility of the liquid to the first order. The numerical tools are an initial value problem solver (shooting method implemented in CUDA C to exploit the high numerical computing power of GPUs) and a boundary value problem solver combined with the pseudo-arch length continuation technique (AUTO). These advanced numerical techniques of nonlinear science provide a better insight into the highly damped bubble oscillations than the previous studies, see e.g. [43].

2. Mathematical model

The employed bubble model is the same as in our previous paper [26], thus here, it is summarized briefly. The modified form [22] of the Keller–Miksis equation [49], which describes the evolution of the bubble radius $R(t)$ in time is

$$\left(1-\frac{\dot{R}}{c_L}\right)R\ddot{R}+\left(1-\frac{\dot{R}}{3c_L}\right)\frac{3}{2}\dot{R}^2 \;=\; \left(1+\frac{\dot{R}}{c_L}+\frac{R}{c_L}\frac{d}{dt}\right)\frac{(p_L-p_\infty)}{\rho_L}, \quad (1)$$

where c_L is the sound velocity in the liquid, ρ_L is the density of the liquid, and the dot stands for the derivative with respect to time. The pressure far away from the bubble

$$p_\infty(t) = P_\infty + p_A \sin(\omega t) \quad (2)$$

consist of a static and a periodic component, where P_∞ is the ambient pressure, p_A is the pressure amplitude and ω is the angular frequency of the excitation.

The pressure inside the bubble is the sum of the partial pressures of the non-condensable gas p_G and vapour p_V. The liquid pressure at the bubble wall is p_L. The three kinds of pressures are connected by the dynamic

mechanical equilibrium at the interface:

$$p_G + p_V = p_L + \frac{2\sigma}{R} + 4\mu_L \frac{\dot{R}}{R}, \tag{3}$$

where σ is the surface tension and μ_L is the liquid dynamic viscosity.

The gas content obeys a simple polytropic state of change

$$p_G = p_{G0} \left(\frac{R_0}{R} \right)^{3n}, \tag{4}$$

where R_0 and p_{G0} are the reference radius and pressure, respectively. The polytropic exponent is $n = 1.4$ assuming adiabatic gas behaviour.

2.1. Parameters and material properties

During the computations, the ambient pressure $P_\infty = 1\,\mathrm{bar}$ was constant. The ambient temperature T_∞, which is one of the control parameter, specifies all the liquid material properties (the pressure dependence can be negligible), which were determined by means of the experiments of the Dow Chemical Company. The tabulated values are summarized in Appendix C.

The bubble size is given by the equilibrium radius $R_E = 0.1\,\mathrm{mm}$ of the unexcited system ($p_A = 0$). This is a common way to prescribe the size of the bubble. Now, if the reference radius is set to $R_0 = R_E$ then the gas reference pressure can be expressed as

$$p_{G0} = \frac{2\sigma}{R_E} - (p_V - P_\infty)\,. \tag{5}$$

The two remaining parameters are related to the acoustic irradiation, namely, the pressure amplitude p_A and the angular frequency ω. The angular frequency is normalized with the undamped linear eigenfrequency [2]

$$\omega_E = \sqrt{\frac{3n\,(P_\infty - p_V)}{\rho_L R_E^2} + \frac{2\,(3n-1)\,\sigma}{\rho_L R_E^3}} \tag{6}$$

of the system, which defines the relative frequency as

$$\omega_R = \frac{\omega}{\omega_E}. \tag{7}$$

During the computations, dimensionless variables were used: dimensionless bubble radius $x_1 = R/R_E$, dimensionless time $\tau = t/\,(2\pi/\omega)$ and dimensionless bubble wall velocity $x_2 = x_1'$, where the $'$ stands for the derivative with respect to τ. The dimensionless equation system is given in Appendix A.1 in detail.

3. Numerical tools

3.1. Initial value problem solver and Poincaré section

Due to the strong nonlinearity of the Keller–Miksis equation, analytical solutions are not known to be exist, but numerical solutions can be easily obtained. The simplest method is to use an initial value problem (IVP) solver with suitable initial conditions and integrate the system forward in time. After several acoustic cycles, the transient trajectory converges to a stable solution called attractor. Since the bubble is periodically excited, the simplest solution is a closed periodic orbit. If the converged trajectory repeats itself after m acoustic cycles, it is called period m orbit. Figure 1 shows different periodic attractors in the dimensionless x_1-x_2 phase plane. The red, blue and orange curves show period 1, 2 and 3 solutions calculated at pressure amplitudes 1.5, 3 and 3.5 bar, respectively.

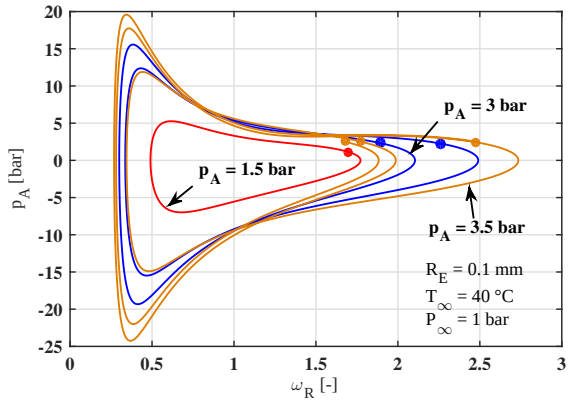

Figure 1: Examples of period 1 (red), 2 (blue) and 3 (orange) attractors in the dimensionless phase plane at pressure amplitudes 1.5, 3 and 3.5 bar, respectively. The dots denote the points of the Poincaré section.

As one can see from Fig. 1, the trajectories of the periodic solutions can intersect themselves and each other in the phase plane producing overcrowded figures. To avoid this difficulty, only some characteristic properties of the solutions were recorded such as the periodicity or the points of the Poincaré map obtained by sampling the continuous trajectory at the end of every acoustic period. The points of the Poincaré section of the periodic orbits in Fig. 1 are denoted by the dots. The period of the bubble oscillation may even tends to infinity never repeating itself. This type of solution called chaotic

attractor. An example is given in Fig. 2 by its 10000 number of Poincaré points.

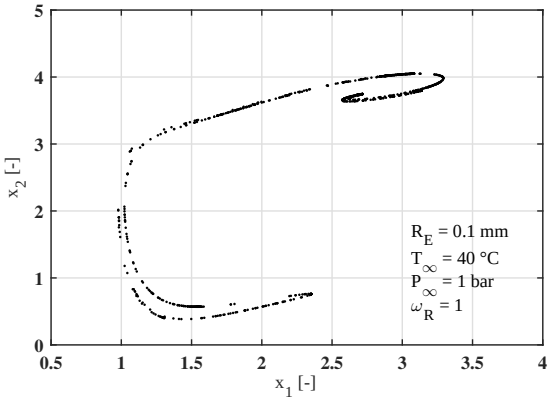

Figure 2: An example for a chaotic attractor in the dimensionless phase plane. The continuous trajectory is omitted; only the points of the Poincaré map are presented by the dots.

3.2. High resolution bi-parametric plots

A very efficient tool to investigate the bifurcation structure of nonlinear systems is to solve millions of IVPs and create high resolution bi-parametric plots [50–74]. For instance, the top panel of Fig. 3 shows the periods of the found attractors up to period 6 as a function of the relative frequency ω_R and pressure amplitude p_A at temperature $T_\infty = 55\,^\circ\mathrm{C}$ (period 7 or higher periods including chaos can be found in the white domains). The resolution of the parameter plane is 501×651. At each parameter pair, 3 number of randomized initial conditions are applied to reveal the co-existing attractors. Therefore, this single plot contains approximately 1 million IVPs. In order to obtain such high-resolution parameter scan within reasonable time, the exceptionally high floating point processing power of our video-card (Nvidia GTX GeForce Titan Black, Kepler architecture, 1707 double precision GFLOPS) is exploited. The numerical algorithm is the adaptive Runge–Kutta–Cash–Karp method with embedded error estimation of orders 4 and 5 [75]. The computational time of Fig. 3 top is only 20 hours. The series of such high resolution plots at various ambient temperatures T_∞ shall help to explore the evolution of the bifurcation superstructure with varying damping factror in the p_A-ω parameter plane, see Section 4 for details.

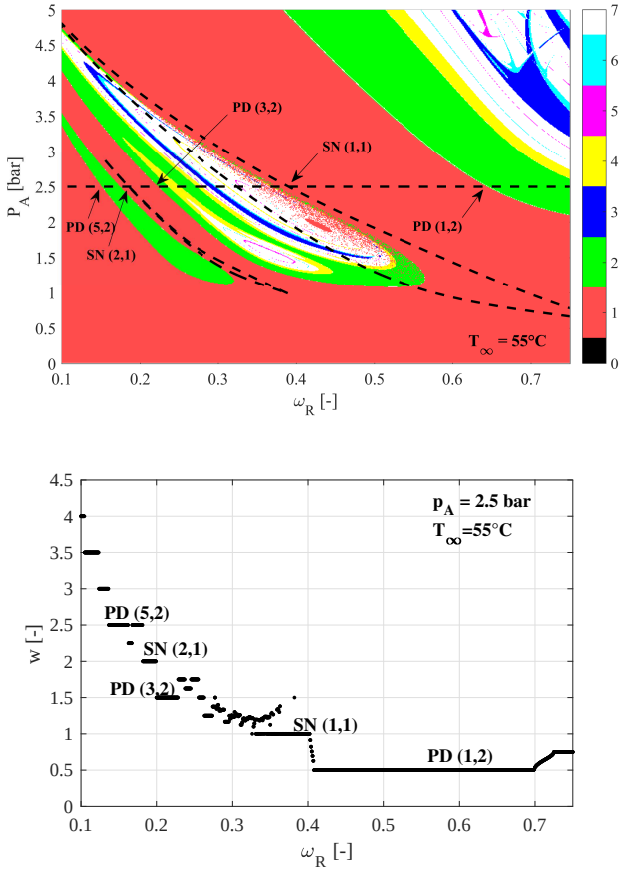

Figure 3: Top panel: high resolution bi-parametric plots where the periods of the found attractors are presented as a function of the relative frequency ω_R and the pressure amplitude p_A up to period 6. The dashed curves are saddle-node bifurcations computed by AUTO. The order of the resonances are marked by $SN/PD(n,m)$. Bottom panel: winding number spectra as a function of the relative frequency ω_R at pressure amplitude $p_A = 2.5\,\mathrm{bar}$.

3.3. The boundary value problem solver AUTO

An efficient way to compute and obtain periodic orbits directly is to use a boundary value problem (BVP) solver. In the present study, the AUTO continuation and bifurcation analysis software was used, see Doedel et al. [76]. AUTO is insensitive to the stability of the corresponding periodic orbit; therefore, its evolution can be easily traced with respect to a control parameter by means of the pseudo-arc length continuation technique. Along such a bifurcation curve, the bifurcation points (saddle-node SN and period

doubling PD) can be detected where the stability of the periodic solution changes. Moreover, AUTO is capable to track down these detected points in a two-dimensional parameter space (codim 2 curves). Some of the codim 2 saddle-node bifurcations found are shown in the top of Fig. 3 by the closed dashed curves and marked by $SN(1,1)$ (main resonance) and $SN(2,1)$ (first harmonic resonance).

In bubble dynamics, AUTO was also used by Fyrillas and Szeri [4] for the rectified diffusion problem and Lauterborn and his co-workers to investigate the bifurcation patterns of a single bubble [22]. Moreover, it is intensively used in other branches of science, for instance, in the study of the stability of compression systems and pressure relief valves [77–79]. A brief description of the numerical technique of AUTO is given in Appendix B.

3.4. Winding number and torsion number

The winding and the torsion numbers are used to describe the topological changes of the local flow near bifurcation points [44–48, 71, 80–82]. They describe the average angular velocity and number of twists around a periodic orbit of a nearby (perturbed) trajectory. An efficient way to compute them is to solve the dynamical system together with its linearized counterpart, since the linearized equations contain all the information about the neighbouring orbits.

With the aid of the torsion frequency

$$\Omega = \lim_{t\to\infty} \frac{\alpha(t) - \alpha(0)}{t}, \tag{8}$$

which determines the average angular velocity, the generalized winding number can be defined as

$$w = \frac{\Omega}{\omega}, \tag{9}$$

where $\alpha(t)$ is the accumulated angle measured from an arbitrarily chosen initial angle $\alpha(0)$. Definition (9) is valid both for periodic and aperiodic (e.g. chaotic) solutions.

Figure 3 bottom shows the computed winding number spectra corresponding to the horizontal dashed line in the top panel of Fig. 3 at $p_A = 2.5\,\mathrm{bar}$. Observe that the winding number w does not change near a bifurcation point. For instance, the winding number $w = 0.5$ is constant in a wide range of the control parameter around the period-doubling bifurcation at $\omega_R = 0.63$. We shall see in the next sections that this invariant property

makes the winding number an efficient tool in the investigation of the topology of bifurcation patterns. The numerical technique to solve the linearized system and determine the winding number (9) is given in Appendix A.2.

For periodic orbits, the torsion number n can be derived as

$$n = w \cdot m, \tag{10}$$

where m is the period of the solution. The two quantities n and m can be associated to each bifurcation point. Therefore, the aforementioned period-doubling point (first subharmonic resonance) can be characterized by its winding number $w = 0.5$, or by its order $PD(1, 2)$ or simply $1/2$ as well. Observe that in the winding number spectra, other resonances can be recognizable by their corresponding plateaus. For example, the harmonic resonances of orders $SN(1, 1)$ and $SN(2, 1)$; and the ultraharmonic resonances of orders $PD(3, 2)$ and $PD(5, 2)$.

4. Highly damped resonances

In our previous paper [26], the effect of the viscous damping on the resonances through the alteration of the liquid temperature T_∞ was studied by means of magnification diagrams of frequency response curves at two different pressure amplitudes. The temperature was varied between 20 °C and 70 °C; the corresponding dynamic viscosities are 1.41 Pa s and 0.0506 Pa s, respectively (see Tab. C.2). Observe that there is an almost two orders of magnitude difference between the lowest and the highest investigated viscosities. It was found that below the critical temperature $T_\infty = 27.44\,°\mathrm{C}$, the system behaves like an overdamped oscillator and no resonance peaks are presented in the frequency response diagrams. Increasing the temperature (decreasing the damping rate), several peaks of harmonic resonances emerges one after another resulted in a similar structure computed first by Lauterborn for water [17] and later on by many others [43, 83–85].

The resonance phenomenon, however, is two dimensional in nature in the excitation amplitude and frequency parameter plane. Therefore, series of high-resolution bi-parametric scans are computed with p_A and ω_R as control parameters at several liquid temperatures T_∞ varied between 20 °C and 70 °C with $\Delta T_\infty = 5\,°\mathrm{C}$ increment. Out of the 11 number of plots, only 6 are presented in Fig. 4. The technical parameters (colour codes, resolution of the parameter plane and the number of the initial conditions) are the same as in case of the top panel of Fig. 3.

The sequence of diagrams in Fig. 4 gives a good insight into the evolution of the complex bifurcation superstructure develops from a very simple state where only period 1 solutions dominate the parameter space (Fig. 4A). The basic bifurcation scenario is the appearance of harmonic $SN(x,1)$ and ultraharmonic $PD(x,2)$ resonances via a "bubbling" mechanism which means the formation of closed bifurcation curves at a certain value of the liquid temperature, see Figs. 4B-F. Here x is a positive integer number. Each of the $SN(x,1)$ resonances are composed by a pair of saddle-node curves connected by a pair of cusp bifurcation points (see e.g. Fig. 4B). They are marked by the dashed lines and computed by the boundary value problem solver AUTO. This additional computation is mandatory since the boundary of the domains of co-existing period 1 attractors (due to the presence of hysteresis) is difficult to visualize in a periodicity diagram. On the contrary, the evolution of the ultraharmonic resonances of orders $PD(x,2)$ can be easily followed by the borders of the red and green domains.

The structure of the $SN(x,1)$ and $PD(x,2)$ resonances in the p_A-ω_R two-dimensional parameter plane is well-known for water [15, 22], where the corresponding bifurcation curves are also computed with a boundary value problem solver. Since water has much lower viscosity (approx. $0.001\,\mathrm{Pa\,s}$), these papers demonstrate an already well developed structure. By means of winding numbers, these resonances are organized according to the first two stages of a Farey-tree [15, 82], see also the first two rows of Fig. 5. The first stage composed by the harmonic resonances $SN(x,1)$ and the subsequent stages can be computed by the Farey-adding. That is, between resonances of orders (n_1,m_1) and (n_2,m_2) there must be a resonance of order $(n_3,m_3) = (n_1+n_2, m_1+m_2)$.

Examining the high resolution bi-parametric plots computed at several liquid temperatures T_∞, it has been found that the $SN(x,1)$ and $PD(x,2)$ resonances appear in a well-ordered manner with increasing temperature. First, the $SN(1,1)$ main resonance emerges followed by the alternating birth of $PD(x,2)$ and $SN(x,1)$ structures according to the path denoted by the arrows between the elements in the first two stages of the Farey-tree in Fig. 5. The common origin of these resonances (each is bifurcated from the period 1 domain) can explain this well-ordered organization. By investigating the winding number spectra as a function of the relative frequency ω_R at $T_\infty = 30\,^\circ\mathrm{C}$ and at $p_A = 1.5\,\mathrm{bar}$ (Fig. 6), the traces of these resonances can already be detectable. Although bifurcations do not exist in the whole domain of the control parameter, the cascade of plateaus of the staircase shaped function

are good indicators for the forthcoming bifurcations marked by red labels. In this sense, the scenario of the appearance of resonances is like stepping upward in the staircase starting from $SN(1,1)$.

The harmonic $SN(x,1)$ and the ultraharmonic $PD(x,2)$ resonances form the exoskeleton of the whole bifurcation structure, since every other bifurcation scenarios take place inside the green domains. Moreover, the bifurcation patterns inside the $PD(x,2)$ curves are self-similar; therefore, only the $PD(3,2)$ domain will be investigated in detail.

Two different period doubling cascade can be observed inside the $PD(3,2)$ area appeared via the period "bubbling" mechanism, which are the first stage of the bifurcation process. At $T_\infty = 45\,^\circ$C, only the period 4 domain of order $PD(5,4)$ exists shown by a yellow bubble in Fig. 4C. Increasing the temperature up to $T_\infty = 50\,^\circ$C (Fig. 4D), in this domain a complete Feigenbaum period-doubling cascade takes place resulted in a large white chaotic bubble in which a complex structure of periodic windows emerges. In parallel, the second period doubling sequence also appears initiated by the curve $PD(7,4)$, in which a similar scenario takes place as in case of $PD(5,4)$ demonstrated in Fig. 4E (generation of periodic windows immersed in a large white chaotic bubble). These two chaotic bubbles can be better seen in the magnification shown in Fig. 7C at $T_\infty = 52\,^\circ$C.

It is well known that two kinds of period doubling sequences exist in terms of winding numbers [13, 86] described by the expression

$$w_n = w_0 \pm \frac{(-1/2)^n - 1}{3m_0}, \tag{11}$$

where w_0 is the initial winding number of the first period doubling curve, $m_0 = 1$ is the initial periodicity (the whole period doubling scenario is originated from the period 1 domain) and w_n is the winding number of the n^{th} subsequent PD curves. This correlates very well with our results, since $w_{2,+} = 1.25$ ($PD(5,4)$) and $w_{2,-} = 1.75$ ($PD(7,4)$).

Let us concentrate now on the inner structure of the white chaotic bubble corresponding to the bifurcation curve $PD(5,4)$. The found periodic bands continue to build up the Farey-tree between the members 3/2 and 1/1. For this purpose, another series of high resolution bi-parametric plots are computed at ambient temperatures $T_\infty = 48\,^\circ$C, $50\,^\circ$C, $52\,^\circ$C and $55\,^\circ$C shown in Fig. 7. Each subplot magnifies different part of the $PD(5,4)$ domain and has different numerical setups summarized in the caption of the figure.

Interestingly, not the period 3 resonance of order $SN(4,3)$ appears first during the increase of the temperature (although this element sits in the next, third stage in the Farey-tree), but many other periodic windows with high periods. At $T_\infty = 48\,^\circ$C, for instance, the periodic windows $SN(10,7)$ and $SN(7,5)$ are already presented in the investigated parameter space; and the resonance $SN(4,3)$ are generated only after the existence of the solution $SN(7,5)$, compare Fig. 7A and B. Consequently, this part in the Farey-tree builds up in a bottom-top approach, see the arrows from 10/7 to 4/3 in Fig. 5. Inside the $SN(4,3)$ bubble, the Farey-tree builds up in another way around. First, the $SN(5,4)$ window is generated approximately at $52\,^\circ$C (Fig. 7C) followed by the $SN(6,5)$ and the $SN(7,6)$ orbits one after another shown Fig. 7D, which is a top-bottom approach (see again the corresponding arrows in Fig. 5). This bottom-top-bottom build-up of the Farey-tree has consequences on how we are thinking about the energy mixing process of nonlinearity, which is discussed in more details in Section 5.

Although the aforementioned orbits fit very well into the Farey ordering, there are lots of other orbits do not marked in Fig. 7 which does not. Thus, there must be other rules like the period tupling mechanism [87] governed by homoclinic tangencies of the stable and unstable manifolds of saddle points. The detailed investigation of these other possibilities are beyond the scope of the present paper. Moreover, it is reasonable to assume that there are other scenarios in the Farey-tree built up in the same bottom-top-bottom manner. Similarly, it is reasonable to assume that the organization of the periodic orbits inside the $PD(7,4)$ bubble (orbits in the Farey-tree between the resonances 2/1 and 3/2) is the same as inside $PD(5,4)$. Since the resonance $SN(8/5)$ (Fig. 7D, $T_\infty = 55\,^\circ$C) appears before the resonance $SN(5/3)$ which can be seen only at $T_\infty = 60\,^\circ$C in Fig. 4E.

The discussion above describes the fine structures inside a single chaotic bubble. In fact, inside the domain enclosed by the resonance curve $PD(3/2)$, a complex cascade of bubbling mechanism takes place each giving birth to a similar chaotic bubble. For instance, at $T_\infty = 55\,^\circ$C in Fig. 7D, two new period 8 bubbles emerge via the period doublings $PD(13/8)$ and $PD(11/8)$; or the two chaotic bubbles appears inside the period 3 domain of $SN(5/4)$ which can be clearly seen in Fig. 4E-F. From this bubbling mechanism, another "new" Farey-tree can be composed. The topology is the same as shown in Fig. 5, but it partially consists of different orbits.

The additional series of high resolution bi-parametric maps are presented in Fig. 8 which help to understand the organization of the bubbling cascade.

Again, the different numerical setups are summarized in the caption of the figure. At $T_\infty = 55\,^\circ$C in Fig. 8A, only the period 3 domain of $SN(4,3)$ is presented from the third stage of the Farey-tree. Its counterpart ($SN(5/3)$) appears at slightly higher temperature, approximately at $T_\infty = 57\,^\circ$C shown in Fig. 8B. At this stage, the "new" Farey-tree composed by the same members as the one related to the fine substructure of the chaotic bubble discussed in Fig. 7. The forthcoming stages, however, will be different. A good example is the two stripes of period 5 orbits in the upper right part of Fig. 8B which have the same order of $SN(6,5)$. Between them there is a period 4 band with order $SN(5/4)$. The upper $SN(6,5)$ and the $SN(5/4)$ orbits are the members of the fine substructure of the chaotic bubble depicted by the flow of arrows from 10/7 to 8/7 in Fig. 5. Therefore, they are also depicted in Fig. 7D. On the contrary, the lower $SN(6,5)$ band is the first member of the "new" Farey-tree at the fifth stage. In addition, a new period 6 bubble ($PD(9,6)$) appears in the period 3 domain of order $SN(4/3)$. Therefore, inside this period 3 region there is altogether two period doubling bifurcations curves: $PD(7,6)$ (large) and $PD(9,6)$ (small). Observe that this two period doubling scenarios also obey the rule described by equation (11).

Increasing the temperature to $T_\infty = 63\,^\circ$C (Fig. 8C), the aforementioned $PD(9,6)$ curve become larger and inside it a new period 5 ring evolves with order $SN(7,5)$, which is the second member of the fifth stage of the "new" Farey-tree. Moreover, inside the $SN(5,3)$ period 3 domain, two chaotic bubbles emerge via the two types of period doubling cascade. The corresponding first period doubling bifurcations are $PD(9,6)$ and $PD(11,6)$. Inside each of these chaotic bubbles, period 5 rings are formed at $T_\infty = 65\,^\circ$C. Their orders are $SN(8,5)$ and $SN(9,5)$; thus, all the orbits in the fifth, period 5 stage of the Farey-tree have been found, see also Fig. 5. It is still an open question how the elements in the fourth stage ($PD(7,4)$ and $PD(5,4)$) fit into the bubbling scenario. Probably, they are the period doubling curves at the boundary of the green and yellow domains, see e.g. Fig. 8A. In order to understand the above described bubbling mechanism, Fig. 9 shows a pictogram about the bubbles, their periods in parenthesis and their orders by arrows. Increasing the temperature (decreasing the damping factor), it is very probable that the Farey-tree continues to build up with solutions of higher periods.

The last issue have to be addressed is that the two new period 8 bubbles of orders $PD(13/8)$ and $PD(11/8)$ in Fig. 7A does not fit into the structure depicted by the pictogram in Fig. 9. They simply comes from a period

doubling mechanism already investigated in details by Parlitz [45]; therefore, here it is discussed very briefly. By the composition of Fig. 7a-b of that paper, another pictogram can be created shown in Fig. 10 (omitting the inner saddle-node curves). The basic period and the torsion number of the outer bifurcation curve (in general it can be either a SN or a PD curve) are denoted by m and n, respectively. For our specific case the order of the outer curve is $PD(3,2)$; that is, $n = 3$ and $m = 2$. Observe the remarkable similarity between Fig. 9 and Fig. 10. Parenthetically, this period doubling scenario hold for other basic periodicities. See for instance, the period 3 domain of order $SN(5,3)$ in Fig. 8C.

5. Discussion

The extensive study of many nonlinear dynamical systems has revealed many features of their bifurcation structures in the last decades. It has been found that the topology of these structures (organization of periodic and chaotic domains in single and multi-dimensional parameter space) can be characterized by Farey-trees. It seems to be so universal that even the Feigenbaum period doubling scenario [86] and the period tupling mechanism [87] can also be derived as a Farey-tree.

The Farey-tree, however, is not unique. More precisely, the topology of the complete bifurcation superstructure, e.g. in the two dimensional excitation amplitude and frequency parameter space of a forced nonlinear oscillator, cannot be described by a single Farey structure. For instance, in case of the aforementioned period tupling phenomenon [87], each of the main bifurcation structure and its substructures at various levels are governed by different Farey-trees resulted in a cascade of nested Farey objects. It is similar in the present study as well. The main period bubbling scenario presented in Fig. 9 is organized as a Farey-tree. In parallel, the period doubling cascade described by Fig. 10 appeared also via a bubbling mechanism can also be derived as a Farey-tree (see the again the publication [86]). Finally, the fine substructure inside each of this bubble is also obeys a Frey-tree structure. Consequently, the topology of the bifurcation structure in the region of harmonic resonances of our bubble model can also be described by nested Farey objects.

It is generally accepted, that Farey-trees describe energy transfer from harmonic resonances to higher order resonances [88]. This is the frequency mixing effect of nonlinearity. The Farey structures, however, are not com-

pleted. Due to the presence of dissipation (in our case the main dissipation mechanism comes from the liquid viscosity), the build-up of the Farey-trees must stop at a certain stage preventing the further energy transfer. This is a similar mechanism take place in a turbulent fluid flow where the energy transfer from large eddies to smaller vortices stops at the level called Kolmogorov scale (also due to the dissipation).

The main advantage of our approach presented throughout this study (investigation of the system from high to low dissipation), is that the effect of dissipation on the evolution of the bifurcation superstructure and its corresponding Farey-trees can be clearly followed. Interestingly, it has been found that there are substructures in which the related Farey-tree builds-up not from a top to bottom (low periods to high periods) but from a bottom-top-bottom (high periods appears first followed by low periods and again continues with high periods) approach. This means that in the energy cascade, the energy is immediately transferred to resonances of very high periodicities.

Acknowledgements

The research described in this paper was supported by the Hungarian Scientific Research Fund – OTKA, Grant No. K81621.

This paper was supported by the János Bolyai Research Scholarship of the Hungarian Academy of Sciences.

Appendix A. Initial value problem solver

Appendix A.1. Dimensionless equation system

By applying the dimensionless variables, the modified Keller–Miksis equation 1 can be rewritten as a system of two first order, dimensionless differential equations:

$$x_1' = x_2, \tag{A.1}$$

$$x_2' = \frac{N}{D}, \tag{A.2}$$

where

$$
\begin{aligned}
N =& \frac{1}{x_1}\left(C_2 - C_5\sin(2\pi\tau)\right) + \frac{x_2}{x_1}\left(C_7 - C_8\sin(2\pi\tau)\right)\\
&+ \left(\frac{1}{x_1}\right)^{3n+1}\left(C_1 + x_2 C_6\right) - \frac{1}{x_2^2}\left(C_3 + x_2 C_4\right)\\
&- C_9\cos(2\pi\tau) - \frac{x_2^2}{x_1}\left(\frac{3}{2} - \frac{1}{2}x_2 C_{10}\right),
\end{aligned}
\tag{A.3}
$$

and

$$
D = 1 - x_2 C_{10} + \frac{1}{x_1}C_{11}. \tag{A.4}
$$

The constant variables are:

$$
\begin{aligned}
&C_1 = \frac{p^B_{ref}}{p^A_{ref}}, \quad C_2 = \frac{p_v - P_\infty}{p^A_{ref}}, \quad C_3 = \frac{2\sigma}{R_E p^A_{ref}},\\
&C_4 = \frac{4\mu_L\omega}{2\pi p^A_{ref}}, \quad C_5 = \frac{p_A}{p^A_{ref}}, \quad C_6 = (1-3n)\frac{p^B_{ref}}{\mu^A_{ref}},\\
&C_7 = \frac{p_v - P_\infty}{\mu^A_{ref}}, \quad C_8 = \frac{p_A}{\mu^A_{ref}}, \quad C_9 = \frac{p_A}{\mu^B_{ref}},\\
&C_{10} = \frac{R_E\omega}{2\pi c_L}, \quad C_{11} = \frac{4\mu_L}{\mu_{ref}}.
\end{aligned}
\tag{A.5}
$$

The reference properties are:

$$
\begin{aligned}
&p^A_{ref} = \rho_L R_E^2\left(\frac{\omega}{2\pi}\right)^2, \quad p^B_{ref} = \frac{2\sigma}{R_E} - \left(p_V - P_\infty\right),\\
&\mu_{ref} = c_L\rho_L R_E,\\
&\mu^A_{ref} = c_L\rho_L R_E\frac{\omega}{2\pi} = \mu_{ref}\frac{\omega}{2\pi},\\
&\mu^B_{ref} = c_L\rho_L R_E\frac{\omega}{4\pi} = \mu^A_{ref}\frac{1}{2\pi}.
\end{aligned}
\tag{A.6}
$$

According to Eq. (4) and (5), the gas pressure inside the bubble is

$$
p_G = p^B_{ref}\left(\frac{1}{x_1}\right)^{3n}. \tag{A.7}
$$

The pressure outside the bubble at the bubble wall is

$$
p_L = p_G + p_V - \frac{2\sigma}{R_E x_1} - 4\mu_L\frac{\omega x_2}{2\pi x_1}, \tag{A.8}
$$

and the pressure far away from the bubble is

$$p_\infty(\tau) = P_\infty + p_A \sin(2\pi\tau). \tag{A.9}$$

Observe that the period of excitation in the dimensionless system is unity ($\tau_0 = 1$) and the dimensionless excitation frequency is 2π.

Appendix A.2. Linearized equation of motion

In order to compute the torsion of the local flow around a given periodic orbit, two more differential equations need to be added to system (A.1) - (A.2). Let γ denote the periodic orbit associated to the solution of the dimensionless system $\underline{\mathrm{x}}(\tau) = [x_1(\tau), x_2(\tau)]^T$, and let γ' denote the neighboring orbit of γ given by $\underline{\mathrm{z}}(\tau) = \underline{\mathrm{x}}(\tau) + \underline{\mathrm{y}}(\tau)$, where $\underline{\mathrm{y}}(\tau)$ is assumed to be infinitesimally small. The time evolution of $\underline{\mathrm{y}}(\tau)$ is given by the variational equation:

$$y_1' = y_2, \tag{A.10}$$

$$y_2' = \left[\left(\frac{\partial N}{\partial x_1}D - \frac{\partial D}{\partial x_1}N\right)y_1 + \left(\frac{\partial N}{\partial x_2}D - \frac{\partial D}{\partial x_2}N\right)y_2\right]\frac{1}{D^2}. \tag{A.11}$$

The necessary partial derivatives are

$$\begin{aligned}\frac{\partial N}{\partial x_1} &= C_2 - C_5\sin(2\pi\tau) + x_2(C_7 - C_8\sin(2\pi\tau)) - \\ &(-3n+1)\left(\frac{1}{x_1}\right)^{3n+2}(C_1 + x_2C_6) - \frac{2}{x_1^3}(C_3 + C_4x_2) + \\ &\left(\frac{x_2}{x_1}\right)^2\left(\frac{3}{2} + \frac{1}{2}C_{10}x_2\right),\end{aligned} \tag{A.12}$$

$$\begin{aligned}\frac{\partial N}{\partial x_2} &= \frac{1}{x_1}(C_7 - C_8\sin(2\pi\tau)) + \left(\frac{1}{x_1}\right)^{3n+1}C_6 - \frac{C_4}{x_1^2} \\ &- \frac{3x_2}{x_1} + \frac{3x_2^2}{x_1},\end{aligned} \tag{A.13}$$

$$\frac{\partial D}{\partial x_1} = -\frac{C_{11}}{x_1^2}, \tag{A.14}$$

$$\frac{\partial D}{\partial x_2} = -C_{10}. \tag{A.15}$$

Transforming the variational equations Eqs. (A.10)-(A.11) into polar coordinates $y_1 = r \cdot \cos\alpha$ and $y_2 = r \cdot \sin\alpha$, the evolution of r and α with respect to τ can be written as

$$r' = \cos\alpha(r \cdot \sin\alpha + y_2'), \tag{A.16}$$

$$\alpha' = \cos\alpha\frac{y_2'}{r} - \sin^2\alpha. \tag{A.17}$$

By solving differential equations (A.16)-(A.17) together with Eqs. (A.1)-(A.2), the torsion frequency $\Omega(\gamma)$ of orbit γ can be easily obtained. If the initial angle is choosen to be $\alpha_0 = 0$, then the torsion frequency can be calculated by

$$\Omega(\gamma) = \lim_{\tau\to\infty}\frac{|\alpha(\tau)|}{\tau}. \tag{A.18}$$

Since the dimensionless excitation frequency is 2π, the generalized winding number is defined as

$$w(\gamma) = \frac{\Omega(\gamma)}{2\pi}. \tag{A.19}$$

For the numerical simulations, a MATLAB built-in solver was used, which was a 4th order Runge–Kutta scheme with 5th order embedded error estimation.

Appendix B. Boundary value problem solver

An efficient way to compute periodic solutions is to use a boundary value problem (BVP) solver on our second order system

$$\underline{\mathrm{x}}' = \underline{\mathrm{f}}(\underline{\mathrm{x}}, \tau) \tag{B.1}$$

by applying periodic boundary conditions:

$$\underline{\mathrm{x}}(0) = \underline{\mathrm{x}}(\tau_p), \tag{B.2}$$

where $\underline{\mathrm{x}} = [x_1, x_2]^T$, $\tau_p = m\cdot\tau$ is the period of the solution with periodicity m, and $\underline{\mathrm{f}}$ is defined by Eqs. (A.1) and (A.2). In present paper, the AUTO continuation and bifurcation analysis software was used to solve the boundary value problem, see the manual of Doedel et al. [76]. AUTO uses the method of orthogonal collocation with piecewise polynomial and 2-7 collocation points per mesh interval to discretize the boundary value problem. The mesh adapts

automatically to the solution to satisfy the local discretization error. Once a solution is computed, AUTO can trace its evolution with respect to a control parameter by the method of pseudo arc-length continuation technique. This method is capable of following curves containing turning points (folds). The bifurcation points on these curves can also be detected, where the change of the stability takes place. Moreover, AUTO can trace a bifurcation point in a two-parameter (codim 2) space by choosing a secondary control parameter.

Since AUTO can handle only autonomous systems (free of explicit time dependence), two more differential equations decoupled from the original system are required to replace the terms which depend on τ in Eq. (A.3) ($x_3 = \cos(2\pi\tau)$ and $x_4 = \sin(2\pi\tau)$). The decoupled ODEs defined as:

$$\begin{aligned} x_3' &= x_3 + 2\pi x_4 - x_3(x_3^2 + x_4^2), \\ x_4' &= x_4 - 2\pi x_3 - x_4(x_3^2 + x_4^2). \end{aligned} \tag{B.3}$$

Appendix C. Material Properties

Appendix C.1. KDB equation for vapor pressure

The vapor pressure of the glycerine was calculated from the KDB correlation equation ([89]):

$$\ln p_V = A \ln T_\infty + \frac{B}{T_\infty} + C + D T_\infty^2, \tag{C.1}$$

where the coefficients are

$$\begin{aligned} A &= -2.125867 \cdot 10^1, \\ B &= -1.672626 \cdot 10^4, \\ C &= 1.655099 \cdot 10^2, \\ D &= 1.100480 \cdot 10^{-5}. \end{aligned} \tag{C.2}$$

The vapour pressure p_v is in kPa and the ambient temperature T_∞ is in K.

Appendix C.2. Tabulated values of the material properties

The material properties of the glycerine as functions of the ambient temperature are summarized in the following tables (Table C.1 - C.4). These values were taken from the results of Dow Chemical Company. For a given ambient temperature T_∞, the corresponding values of the material properties were calculated with linear interpolation.

Table C.1: Tabulated values of the glycerine density ρ_L as a function of ambient temperature T_∞

$T_\infty\,[^\circ C]$	0	10	15	20	30
$\rho_L\,[kg/m^3]$	1272.7	1267.0	1264.4	1261.3	1255.1
$T_\infty\,[^\circ C]$	40	54	75.5	99.5	110
$\rho_L\,[kg/m^3]$	1249.0	1239.7	1225.6	1209.7	1201.8

Table C.2: Tabulated values of the glycerine dynamic viscosity μ_L as a function of ambient temperature T_∞

$T_\infty\,[^\circ C]$	0	10	20	30	40
$\mu_L\,[Pa\ s]$	12.07	3.9	1.41	0.612	0.284
$T_\infty\,[^\circ C]$	50	60	70	80	90
$\mu_L\,[Pa\ s]$	0.142	0.0813	0.0506	0.0319	0.0213

Table C.3: Tabulated values of the glycerine surface tension σ as a function of ambient temperature T_∞

$T_\infty\,[^\circ C]$	20	90	150
$\sigma\,[m/s]$	0.0634	0.0586	0.0519

Table C.4: Tabulated values of the glycerine sound speed c_L as a function of ambient temperature T_∞

$T_\infty\,[^\circ C]$	10	20	30	40	50
$\rho_L\,[m/s]$	1941.5	1923	1905	1886.5	1869.5

[1] F. G. Blake, The onset of cavitation in liquids, Tech. Rep. 12, Acoust. Res. Lab., Harvard Univ. (1949).

[2] C. E. Brennen, Cavitation and Bubble Dynamics, Oxford University Press, New York, 1995.

[3] O. Louisnard, F. Gomez, Growth by rectified diffusion of strongly acoustically forced gas bubbles in nearly saturated liquids, Phys. Rev. E 67 (3) (2003) 036610.

[4] M. M. Fyrillas, A. J. Szeri, Dissolution or growth of soluble spherical oscillating bubbles, J. Fluid Mech. 277 (1994) 381–407.

[5] L. A. Crum, Acoustic cavitation series: part five rectified diffusion, Ultrasonics 2 (5) (1984) 215–223.

[6] L. A. Crum, Measurements of the growth of air bubbles by rectified diffusion, J. Acoust. Soc. Am 68 (1) (1980) 203–211.

[7] P. Koch, T. Kurz, U. Parlitz, W. Lauterborn, Bubble dynamics in a standing sound field: The bubble habitat, J. Acoust. Soc. Am. 130 (5) (2011) 3370–3378.

[8] J. Holzfuss, Surface-wave instabilities, period doubling, and an approximate universal boundary of bubble stability at the upper threshold of sonoluminescence, Phys. Rev. E 77 (6) (2008) 066309.

[9] T. G. Leighton, The acoustic bubble, Academic press, London, 2012.

[10] R. Mettin, From a single bubble to bubble structures in acoustic cavitation, in: Oscillations, Waves and Interactions: Sixty Years Drittes Physikalisches Institut ; a Festschrift, Universitätsverlag Göttingen, Göttingen, Germany, 2007.

[11] R. Mettin, Bubble structures in acoustic cavitation, in: Bubble and Particle Dynamics in Acoustic Fields: Modern Trends and Applications, Research Signpost, Trivandrum, Kerala, India, 2005.

[12] F. Hegedűs, Stable bubble oscillations beyond Blake's critical threshold, Ultrasonics 54 (4) (2014) 1113–1121.

[13] F. Hegedűs, C. Hős, L. Kullmann, Stable period 1, 2 and 3 structures of the harmonically excited RayleighPlesset equation applying low ambient pressure, IMA J. Appl. Math. 78 (6) (2013) 1179–1195.

[14] W. Lauterborn, T. Kurz, R. Mettin, P. Koch, D. Kröninger, D. Schanz, Acoustic cavitation and bubble dynamics, Arch. Acoust. 33 (4) (2008) 609–617.

[15] U. Parlitz, V. Englisch, C. Scheffczyk, W. Lauterborn, Bifurcation structure of bubble oscillators, J. Acoust. Soc. Am. 88 (2) (1990) 1061–1077.

[16] P. Smereka, B. Birnir, S. Banerjee, Regular and chaotic bubble oscillations in periodically driven pressure fields, Phys. Fluids 30 (11) (1987) 3342–3350.

[17] W. Lauterborn, Numerical investigation of nonlinear oscillations of gas bubbles in liquids, J. Acoust. Soc. Am. 59 (2) (1976) 283–293.

[18] A. Prosperetti, Nonlinear oscillations of gas bubbles in liquids. Transient solutions and the connection between subharmonic signal and cavitation, J. Acoust. Soc. Am. 57 (4) (1975) 810–821.

[19] A. Prosperetti, Nonlinear oscillations of gas bubbles in liquids: steady-state solutions, J. Acoust. Soc. Am. 56 (3) (1974) 878–885.

[20] A. J. Sojahrood, O. Falou, R. Earl, R. Karshafian, M. C. Kolios, Influence of the pressure-dependent resonance frequency on the bifurcation structure and backscattered pressure of ultrasound contrast agents: a numerical investigation, Nonlinear Dyn. 80 (1-2) (2015) 889–904.

[21] A. J. Sojahrood, M. C. Kolios, Classification of the nonlinear dynamics and bifurcation structure of ultrasound contrast agents excited at higher multiples of their resonance frequency, Phys. Lett. A 376 (33) (2012) 2222–2229.

[22] W. Lauterborn, T. Kurz, Physics of bubble oscillations, Rep. Prog. Phys. 73 (10) (2010) 106501.

[23] S. Behnia, A. J. Sojahrood, W. Soltanpoor, L. Sarkhosh, Towards classification of the bifurcation structure of a spherical cavitation bubble, Ultrasonics 49 (8) (2009) 605–610.

[24] S. Behnia, A. J. Sojahrood, W. Soltanpoor, O. Jahanbakhsh, Nonlinear transitions of a spherical cavitation bubble, Chaos Solitons Fract. 41 (2) (2009) 818–828.

[25] S. Behnia, A. J. Sojahrood, W. Soltanpoor, O. Jahanbakhsh, Suppressing chaotic oscillations of a spherical cavitation bubble through applying a periodic perturbation, Ultrason. Sonochem. 16 (4) (2009) 502–511.

[26] F. Hegedűs, K. Klapcsik, The effect of high viscosity on the collapse-like chaotic and regular periodic oscillations of a harmonically excited gas bubble, Ultrason. Sonochem. 27 (2015) 153–164.

[27] R. Varga, G. Paál, Numerical investigation of the strength of collapse of a harmonically excited bubble, Chaos Solitons Fract. 76 (2015) 56–71.

[28] G. Simon, P. Cvitanovic, M. T. Levinsen, I. Csabai, A. Horváth, Periodic orbit theory applied to a chaotically oscillating gas bubble in water, Nonlinearity 15 (1) (2002) 25.

[29] S. Behnia, H. Zahir, M. Yahyavi, A. Barzegar, F. Mobadersani, Observations on the dynamics of bubble cluster in an ultrasonic field, Nonlinear Dyn. 72 (3) (2013) 561–574.

[30] R. Esche, Untersuchung der Schwingungskavitation in Flüssigkeiten, Acta Acust. united Ac. 2 (6) (1952) 208–218.

[31] W. Lauterborn, E. Suchla, Bifurcation superstructure in a model of acoustic turbulence, Phys. Rev. Lett. 53 (24) (1984) 2304–2307.

[32] W. Lauterborn, E. Cramer, Subharmonic route to chaos observed in acoustics, Phys. Rev. Lett. 47 (20) (1981) 1445–1448.

[33] W. Lauterborn, A. Koch, Holographic observation of period-doubled and chaotic bubble oscillations in acoustic cavitation, Phys. Rev. A 35 (4) (1987) 1974–1976.

[34] D. F. Gaitan, L. A. Crum, C. C. Church, R. A. Roy, Sonoluminescence and bubble dynamics for a single, stable, cavitation bubble, J. Acoust. Soc. Am. 91 (6) (1992) 3166–3183.

[35] T. J. Matula, I. M. Hallaj, R. O. Cleveland, L. A. Crum, W. C. Moss, R. A. Roy, The acoustic emissions from single-bubble sonoluminescence, J. Acoust. Soc. Am. 103 (3) (1998) 1377–1382.

[36] A. J. Walton, G. T. Reynolds, Sonoluminescence, Adv. Phys. 33 (6) (1984) 595–660.

[37] R. G. Holt, D. F. Gaitan, A. A. Atchley, J. Holzfuss, Chaotic sonoluminescence, Phys. Rev. Lett. 72 (9) (1994) 1376–1379.

[38] E. M. Englert, A. McCarn, G. A. Williams, Luminescence from laser-induced bubbles in water-glycerol mixtures: Effect of viscosity, Phys. Rev. E 83 (4) (2011) 046306.

[39] R. Toegel, S. Luther, D. Lohse, Viscosity destabilizes sonoluminescing bubbles, Phys. Rev. Lett. 96 (11) (2006) 114301.

[40] K. Yasui, Effect of liquid temperature on sonoluminescence, Phys. Rev. E 64 (1) (2001) 016310.

[41] S. Behnia, F. Mobadersani, M. Yahyavi, A. Rezavand, Chaotic behavior of gas bubble in non-Newtonian fluid: a numerical study, Nonlinear Dyn. 74 (3) (2013) 559–570.

[42] M. S. Plesset, A. Prosperetti, Bubble dynamics and cavitation, Annu. Rev. Fluid Mech. 9 (1) (1977) 145–185.

[43] T. Fujiwara, A. Shima, Nonlinear oscillations of bubbles in compressible hydraulic oils, J. Acoust. Soc. Am. 68 (5) (1980) 1502–1508.

[44] T. Kurz, W. Lauterborn, Bifurcation structure of the Toda oscillator, Phys. Rev. A 37 (1988) 1029–1031.

[45] U. Parlitz, Common dynamical features of periodically driven strictly dissipative oscillators, Int. J. Bifurcat. Chaos 3 (3) (1993) 703–715.

[46] U. Parlitz, W. Lauterborn, Resonances and torsion numbers of driven dissipative nonlinear oscillators, Z. Naturforsch. A 41 (4) (1986) 605–614.

[47] U. Parlitz, W. Lauterborn, Superstructure in the bifurcation set of the Duffing equation $\ddot{x} + d\dot{x} + x + x^3 = fcos(\omega t)$, Phys. Lett. A 107 (8) (1985) 351–355.

[48] C. Scheffczyk, U. Parlitz, T. Kurz, W. Knop, W. Lauterborn, Comparison of bifurcation structures of driven dissipative nonlinear oscillators, Phys. Rev. A 43 (12) (1991) 6495–6502.

[49] J. B. Keller, M. Miksis, Bubble oscillations of large amplitude, J. Acoust. Soc. Am. 68 (2) (1980) 628–633.

[50] C. Bonatto, J. A. C. Gallas, Accumulation horizons and period adding in optically injected semiconductor lasers, Phys. Rev. E 75 (5) (2007) 055204.

[51] C. Bonatto, J. A. C. Gallas, Accumulation boundaries: codimension-two accumulation of accumulations in phase diagrams of semiconductor lasers, electric circuits, atmospheric and chemical oscillators, Philos. T. Roy. Soc. A 366 (1865) (2008) 505–517.

[52] C. Bonatto, J. A. C. Gallas, Y. Ueda, Chaotic phase similarities and recurrences in a damped-driven Duffing oscillator, Phys. Rev. E 77 (2) (2008) 026217.

[53] J. G. Freire, C. Bonatto, C. C. DaCamara, J. A. C. Gallas, Multistability, phase diagrams, and intransitivity in the Lorenz-84 low-order atmospheric circulation model, Chaos 18 (3) (2008) 033121.

[54] C. Bonatto, J. A. C. Gallas, Periodicity hub and nested spirals in the phase diagram of a simple resistive circuit, Phys. Rev. Lett. 101 (5) (2008) 054101.

[55] J. G. Freire, R. J. Field, J. A. C. Gallas, Relative abundance and structure of chaotic behavior: The nonpolynomial BelousovZhabotinsky reaction kinetics, J. Chem. Phys. 131 (4) (2009) 044105.

[56] G. M. Ramírez-Ávila, J. A. C. Gallas, How similar is the performance of the cubic and the piecewise-linear circuits of Chua?, Phy. Lett. A 375 (2) (2010) 143–148.

[57] V. Kovanis, A. Gavrielides, J. A. C. Gallas, Labyrinth bifurcations in optically injected diode lasers, Eur. Phys. J. D 58 (2) (2010) 181–186.

[58] J. G. Freire, J. A. C. Gallas, Non-Shilnikov cascades of spikes and hubs in a semiconductor laser with optoelectronic feedback, Phys. Rev. E 82 (3) (2010) 037202.

[59] J. A. C. Gallas, The structure of infinite periodic and chaotic hub cascades in phase diagrams of simple autonomous flows, Int. J. Bifurcat. Chaos 20 (2) (2010) 197–211.

[60] E. S. Medeiros, S. L. T. de Souza, R. O. Medrano-T, I. L. Caldas, Periodic window arising in the parameter space of an impact oscillator, Phys. Lett. A 374 (26) (2010) 2628–2635.

[61] R. Vitolo, P. Glendinning, J. A. C. Gallas, Global structure of periodicity hubs in lyapunov phase diagrams of dissipative flows, Phys. Rev. E 84 (1) (2011) 016216.

[62] M. A. Nascimento, J. A. C. Gallas, H. Varela, Self-organized distribution of periodicity and chaos in an electrochemical oscillator, Phys. Chem. Chem. Phys. 13 (2) (2011) 441–446.

[63] J. G. Freire, J. A. C. Gallas, SternBrocot trees in cascades of mixed-mode oscillations and canards in the extended Bonhoeffervan der Pol and the FitzHughNagumo models of excitable systems, Phys. Lett. A 375 (7) (2011) 1097–1103.

[64] J. G. Freire, J. A. C. Gallas, Stern-Brocot trees in the periodicity of mixed-mode oscillations, Phys. Chem. Chem. Phys. 13 (26) (2011) 12191–12198.

[65] E. S. Medeiros, S. L. T. de Souza, R. O. Medrano-T, I. L. Caldas, Replicate periodic windows in the parameter space of driven oscillators, Chaos Solitons Fract. 44 (11) (2011) 982–989.

[66] S. L. T. de Souza, A. A. Lima, I. L. Caldas, R. O. Medrano-T, Z. O. Guimarães-Filho, Self-similarities of periodic structures for a discrete model of a two-gene system, Phys. Lett. A 376 (15) (2012) 1290–1294.

[67] L. Junges, J. A. C. Gallas, Frequency and peak discontinuities in self-pulsations of a CO2 laser with feedback, Opt. Commun. 285 (21) (2012) 4500–4506.

[68] A. Sack, J. G. Freire, E. Lindberg, T. Pöschel, J. A. C. Gallas, Discontinuous spirals of stable periodic oscillations, Sci. Rep. 3 (2013) 3350.

[69] C. Cabeza, C. A. Briozzo, R. Garcia, J. G. Freire, A. C. Marti, J. A. C. Gallas, Periodicity hubs and wide spirals in a two-component autonomous electronic circuit, Chaos Solitons Fract. 52 (2013) 59–65.

[70] R. E. Francke, T. Pöschel, J. A. C. Gallas, Zig-zag networks of self-excited periodic oscillations in a tunnel diode and a fiber-ring laser, Phys. Rev. E 87 (4) (2013) 042907.

[71] E. S. Medeiros, R. O. Medrano-T, I. L. Caldas, S. L. T. de Souza, Torsion-adding and asymptotic winding number for periodic window sequences, Phys. Lett. A 377 (8) (2013) 628–631.

[72] R. O. Medrano-T, R. Rocha, The negative side of Chua's circuit parameter space: stability analysis, period-adding, basin of attraction metamorphoses, and experimental investigation, Int. J. Bifurcat. Chaos 24 (09) (2014) 1430025.

[73] R. Rocha, R. O. Medrano-T, Stability analysis and mapping of multiple dynamics of Chuas circuit in full four-parameter spaces, Int. J. Bifurcat. Chaos 25 (13) (2015) 1530037.

[74] D. R. da Costa, M. Hansen, G. Guarise, R. O. Medrano-T, E. D. Leonel, The role of extreme orbits in the global organization of periodic regions in parameter space for one dimensional maps, Phys. Lett. A 380 (18) (2016) 1610–1614.

[75] K. E. Niemeyer, C. J. Sung, Accelerating moderately stiff chemical kinetics in reactive-flow simulations using GPUs, J. Comput. Phys. 256 (2014) 854–871.

[76] E. J. Doedel, B. E. Oldeman, A. R. Champneys, F. Dercole, T. F. Fairgrieve, Y. A. Kuznetsov, R. Paffenroth, B. Sandstede, X. Wang, C. Zhang, AUTO-07P: continuation and bifurcation software for ordinary differential equations, Concordia University, Montreal, Canada (2012).

[77] C. Hős, A. R. Champneys, L. Kullmann, Bifurcation analysis of surge and rotating stall in the mooregreitzer compression system, IMA J. Appl. Math. 68 (2) (2003) 205–228.

[78] C. Hős, A. R. Champneys, Grazing bifurcations and chatter in a pressure relief valve model, Physica D 241 (22) (2012) 2068–2076.

[79] C. J. Hős, A. R. Champneys, K. Paul, M. McNeely, Dynamic behaviour of direct spring loaded pressure relief valves in gas service: II reduced order modelling, J. Loss Prevent. Proc. 36 (2015) 1–12.

[80] S. Y. Kim, Bifurcation structure of the double-well Duffing oscillator, Int. J. Mod. Phys. B 14 (17) (2000) 1801–1813.

[81] R. Gilmore, J. W. L. McCallum, Structure in the bifurcation diagram of the Duffing oscillator, Phys. Rev. E 51 (1995) 935–956.

[82] U. Parlitz, W. Lauterborn, Period-doubling cascades and devil's staircases of the driven van der Pol oscillator, Phys. Rev. A 36 (3) (1987) 1428–1434.

[83] A. Francescutto, R. Nabergoj, Steady-state oscillations of gas bubbles in liquids: Explicit formulas for frequency response curves, J. Acoust. Soc. Am. 73 (2) (1983) 457–460.

[84] A. Shima, S. C. Rajvanshi, T. Tsujino, Study of nonlinear oscillations of bubbles in Powell–Eyring fluids, J. Acoust. Soc. Am. 77 (5) (1985) 1702–1709.

[85] G. Dassie, M. Reali, Dynamics of an oscillating spherical gas/vapor bubble, J. Acoust. Soc. Am. 100 (5) (1996) 3088–3097.

[86] V. Englisch, W. Lauterborn, The winding-number limit of period-doubling cascades derived as Farey-fraction, Int. J. Bifurcat. Chaos 4 (4) (1994) 999–1002.

[87] F. Hegedűs, Topological analysis of the periodic structures in a harmonically driven bubble oscillator near Blake's critical threshold: Infinite sequence of two-sided Farey ordering trees, Phys. Lett. A 380 (9-10) (2016) 1012–1022.

[88] V. Englisch, U. Parlitz, W. Lauterborn, Comparison of winding-number sequences for symmetric and asymmetric oscillatory systems, Phys. Rev. E 92 (2) (2015) 022907.

[89] W. M. Haynes, CRC handbook of chemistry and physics, 95th Edition, CRC press, Internet Version, 2015.

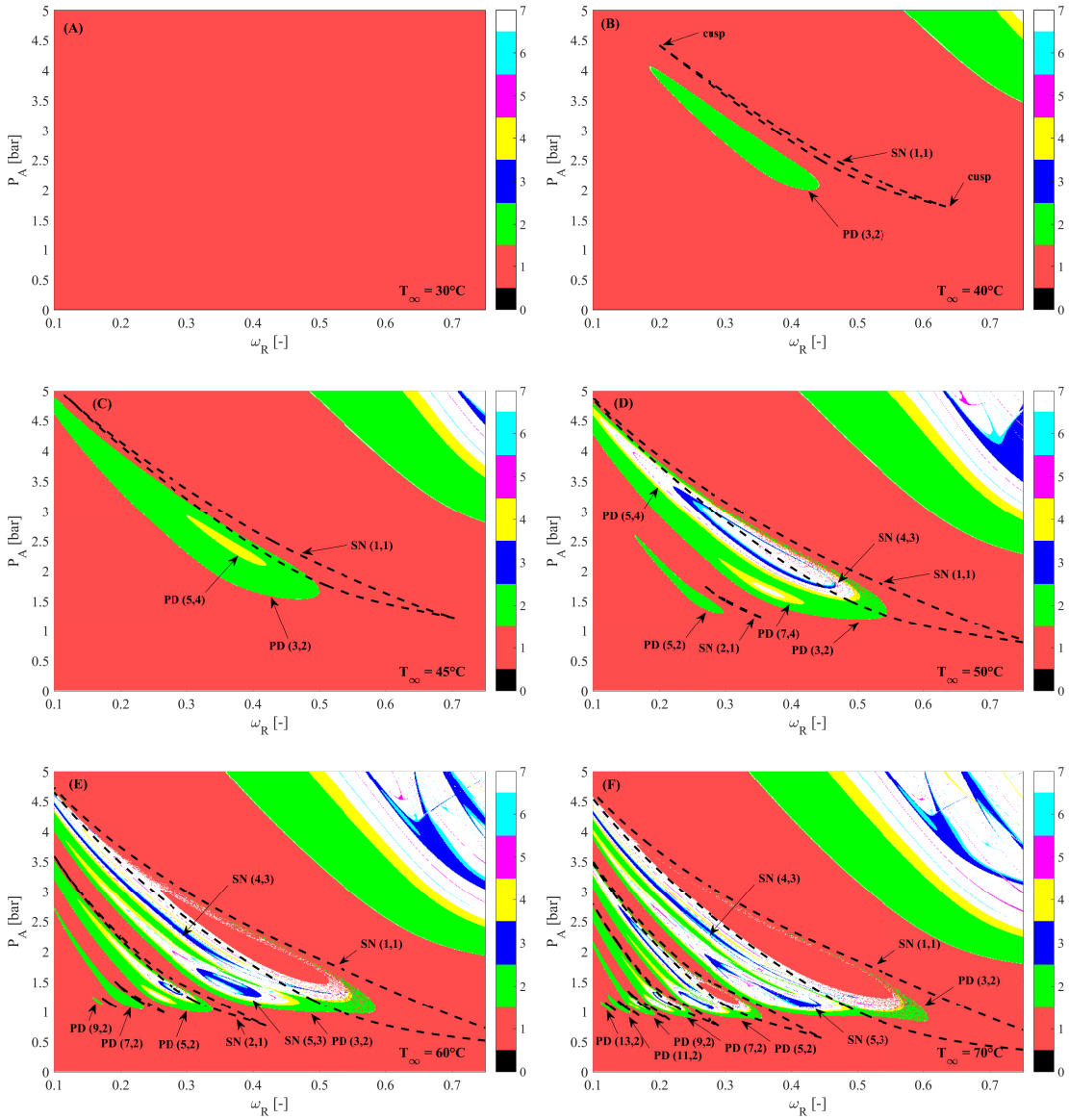

Figure 4: Series of high resolution bi-parametric plots at different temperatures T_∞ where the periods of the found attractors are presented as a function of the relative frequency ω_R and the pressure amplitude p_A up to period 6. The dashed curves are saddle-node bifurcations computed by AUTO. The order of the resonances are marked by $SN/PD(n,m)$.

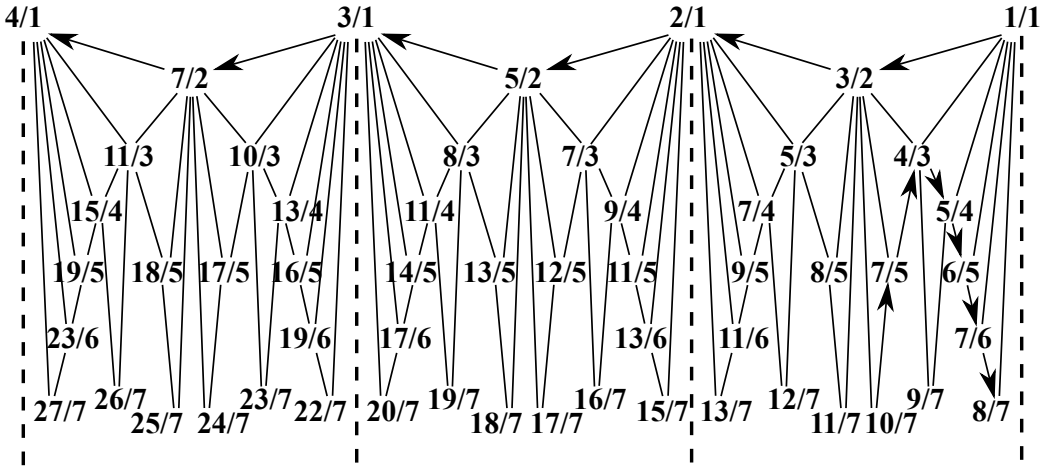

Figure 5: Farey-tree of harmonic and ultraharmonic resonances.

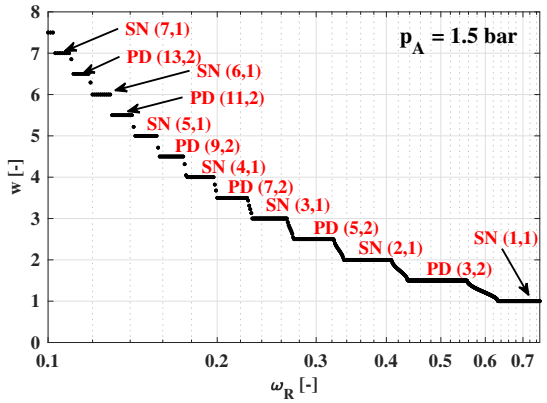

Figure 6: Winding number spectra as a function of the relative frequency ω_R at pressure amplitude $p_A = 1.5\,\text{bar}$ and at temperature $T_\infty = 30\,^\circ\text{C}$.

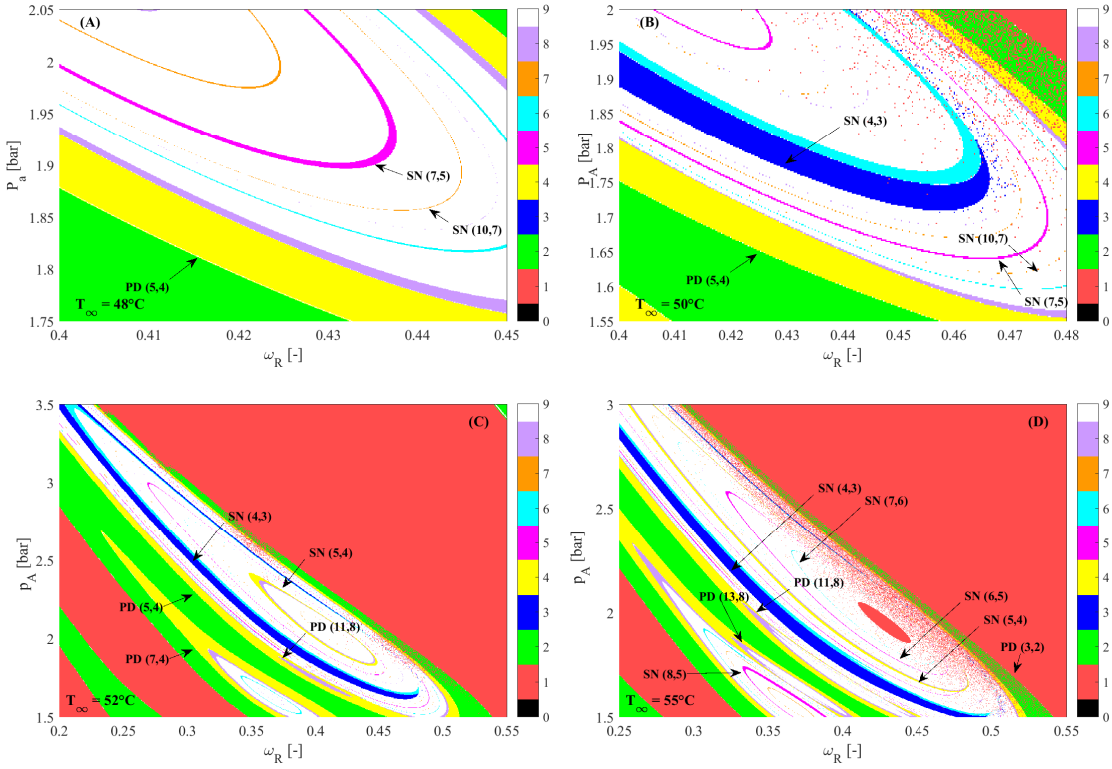

Figure 7: Series of high resolution bi-parametric plots at different temperatures T_∞ where the periods of the found attractors are presented as a function of the relative frequency ω_R and the pressure amplitude p_A up to period 8. The resolution and the number of the initial conditions for subfigures A, B, C and D are $501 \times 501 \times 5$, $226 \times 651 \times 5$, $501 \times 876 \times 5$ and $751 \times 1501 \times 5$, respectively.

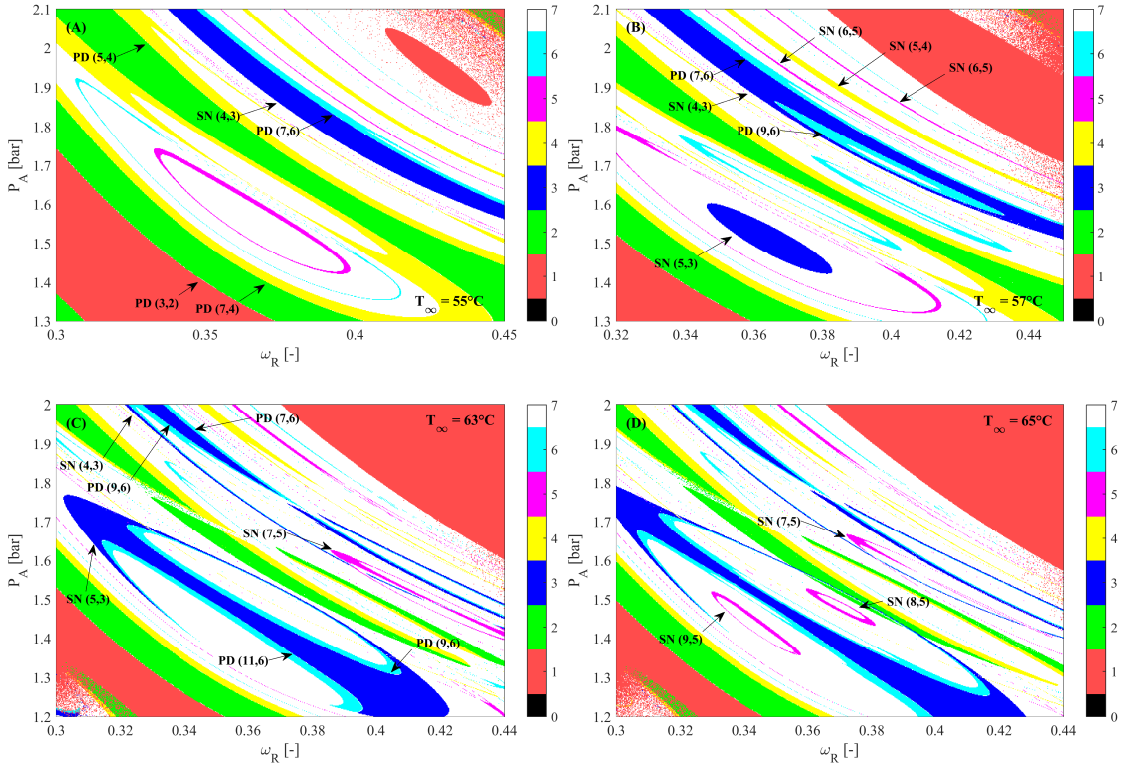

Figure 8: Series of high resolution bi-parametric plots at different temperatures T_∞ where the periods of the found attractors are presented as a function of the relative frequency ω_R and the pressure amplitude p_A up to period 6. The resolution and the number of the initial conditions for subfigures A, B, C and D are $401 \times 751 \times 5$, $401 \times 651 \times 5$, $401 \times 701 \times 5$ and $401 \times 701 \times 5$, respectively.

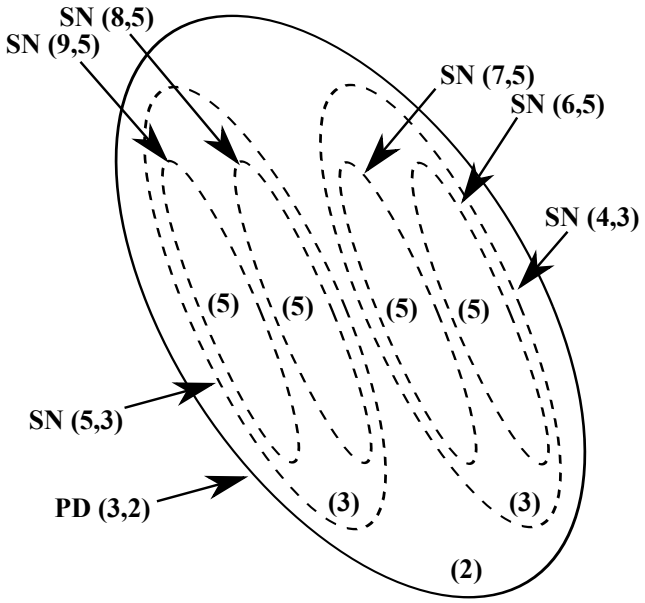

Figure 9: Schematic draw of the main period bubbling mechanism. The periods are denoted in the parenthesis and the orders of the resonances are marked by $SN/PD(n, m)$.

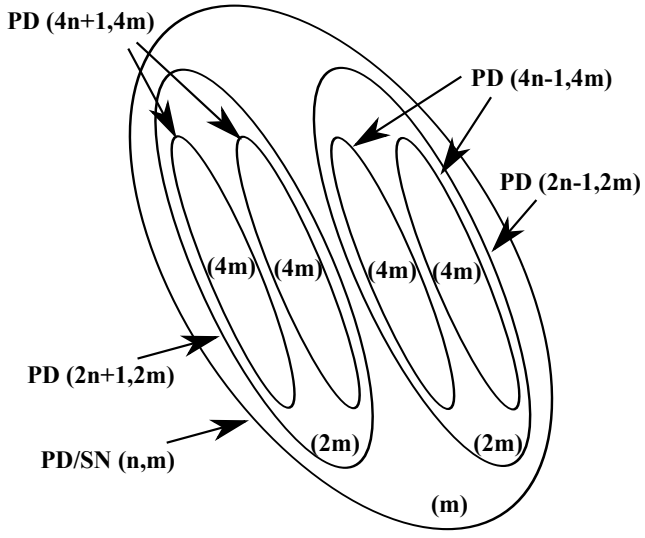

Figure 10: Schematic draw of the period doubling cascade of the period bubbles. The period and the torsion numbers are marked by m and n, respectively.